ISSN 0015-4628, Fluid Dynamics, 2024, Vol. 59, No. 8, pp. 2377–2391. © Pleiades Publishing, Ltd., 2024.

Relativistic Astrospheres of Pulsars and Gamma-Ray Binaries: Modeling of Non-thermal Processes

A. M. Bykov[a],*, A. E. Petrov[a],, and K. P. Levenfish[a]**

[a] *Ioffe Institute, St. Petersburg, 194021 Russia*

**e-mail: byk@astro.ioffe.ru*

***e-mail: a.e.petrov@mail.ioffe.ru*

Received November 14, 2024; revised November 18, 2024; accepted November 19, 2024

Abstract—Relativistic winds of the rotation powered pulsars in binary systems colliding with powerful winds of massive stars are producing astrospheres which are observed as bright gamma-ray sources above TeV photon energies. A long standing problem in high energy astrophysics is the nature of galactic accelerators of particles above PeV energies which are the sources of galactic cosmic rays and are producing PeV regime photons observed by ground based observatories. Recent 2D RMHD modeling revealed that gamma-ray binaries which harbor Gauss-range magnetic field in the winds collision region can accelerate particles above PeV. We present here 2D and 3D simulations of local structure of the winds collision region in gamma-ray binaries and show that in both cases the structures of magnetized flows are favorable for PeV proton acceleration. The strong magnetization of the winds of young massive stars results in prominent anisotropic shape of the relativistic pulsar wind astrosphere and may strongly affect the non-thermal emission of gamma-ray binaries. The sources can be bright in MeV emission regime and can indeed be the sources of PeV energy protons.

Keywords: MHD simulations, gamma-ray binaries, pulsar wind nebulae

DOI: 10.1134/S0015462824605059

INTRODUCTION

Stellar winds (SWs) as the gas and dust outflows accelerated in the upper atmosphere of stars of very different types are observed for a long time as extended astrospheres (see e.g. [1–4](. More than sixty years of study of the heliosphere with direct measurements of the key physical parameters provided unique information on the dynamics of the solar wind. Detailed models of the heliosphere have been created [5–7], taking into account the kinetics of its multiple components (e.g. [8]). Powerful winds of young massive stars and compact relativistic objects, such as black holes and neutron stars, create extended astrospheres visible at many wavelengths. Astrospheres produced by powerful relativistic winds exerted by pulsars appear as bright synchrotron X-ray sources, which are associated with the sources of very high energy gamma-rays. Thus relativistic pulsar winds (PWs) are known as efficient particle accelerators, that energize pulsar wind nebulae (PWNe), converting upto tens percent of wind's power into their non-thermal synchrotron emission from radio to gamma-rays [9]. These objects can be the sources of energetic leptons of the cosmic rays (CRs), they are plausible antimatter factories that can explain the observed CR positron excess in GeV–TeV range (e.g. [10]) and under certain conditions can accelerate CR nuclei well above TeV. Young pulsars with high spin-down luminosity $\dot{E}$, such as Crab pulsar, can even accelerate particles up to PeV energies [11]. The synchrotron emission of such particles in the magnetic fields of PWNe is in MeV–GeV range. The astrospheres of rotation powered pulsars as high energy particle accelerators are discussed in the paper.

In binaries, where the pulsar orbits a massive early-type star, pulsar astrospheres can differ from that of isolated pulsars. The relativistic PW collides there with the powerful wind of massive companion, providing conditions for an efficient acceleration of both leptons and ions. The leptons emit synchrotron and inverse Compton radiation in the strong magnetic field and intense radiation field produced by the companions (see, e.g. [12]). The hadrons can produce gamma-ray photons in interaction with the SW nuclei and stellar optical/ultraviolet photons (e.g. [13–15]). Binaries whose non-thermal emission is bright in gamma-rays are called "the gamma-ray binaries."

The studies of gamma-ray binaries, that in general consist of a compact object (a neutron star or a black hole) and a massive OB star, is a hot issue that still comprises some unsolved problems [16]. Unidentified

yet nature of the compact companion in the gamma-ray binaries LS 5039 [17–19] and LSI 61 303 [20, 21], uncertainties about leptonic or hadronic production of the observed gamma-rays are just a few issues to resolve. Recent detection of 1.4 PeV photon from the source in the Cygnus region by LHAASO gamma-ray observatory [22], that may be associated with the gamma-ray binary PSR J2032+4127, as well as simultaneous detection of sub-PeV gamma-ray flare and neutrino from the same region detected by the Carpet-2 and Ice Cube observatories [23], suggest that these objects might accelerate protons well above PeV.

To address the issues mentioned above an accurate modeling of non-thermal emission of gamma-ray binaries, what assumes simulation of structure of their flows, is required. The hydrodynamical (HD) or magnetohydrodynamical (MHD) simulations of such objects (see, e.g. [24–29]) revealed a complex structure of colliding winds. Most of these models did not account for the effects of magnetic field in the SW which may be especially important for particle acceleration in the short period or high orbital eccentricity gamma-ray binaries.

The Monte Carlo simulations in [15] revealed that acceleration of protons above PeV that is needed to explain the observed sub-PeV photons and neutrino requires magnetic field of the Gauss range in the winds' collision region. Such a field is compatible with the expected SW magnetic fields, since dipole fields above 100 G are found in $\sim$10% of O/B/A massive stars [30, 31]. Indeed, the known orbital parameters of observed gamma-ray binaries assume that their orbital separations are from ~ 0.1 au to tens atomic units [32, 33], or tens-hundreds of typical massive star radii $R_* \sim 10^{12}$ cm. Assuming Parker's model of the SW with $B_{sw} \propto R_*/R$, where R is the distance from the star, one would get $B_{sw} \sim 0.1-10$ G near the compact object.

Studies of gamma-ray binaries as potential pevatrons are of current interest. The Monte Carlo model [15] used simplified assumptions on structure of their flows. More accurate modeling can be performed using MHD-PIC approach, where particles are propagated using the conventional particle-in-cell (PIC) techniques through the simulated system of MHD flows. Bykov et al. [34] provided such simulations in planar geometry. Relativistic MHD (rMHD) simulations by [34] allowed to study the local structure of flows of the gamma-ray binary in the vicinity of the pulsar in the case of a strongly magnetized SW needed for efficient acceleration of PeV particles. It was demonstrated that particle acceleration time in this case is short comparing to the orbital period justifying the local approach.

Whether the planar geometry is applicable for such a problem is an issue to be studied. In the following we provide the comparative analysis of relativistic MHD simulations of gamma-ray binaries performed in the planar and full 3D setups and study the validity of the planar approach. We discuss in details the relativistic outflows in these objects, consider the influence of SW's strong magnetization on their structure and discuss the applications of our results to understanding the non-thermal emission from pulsar's astrospheres.

1. MHD MODEL SETUP

Self-consistent MHD-PIC simulations of flows' structure and particle acceleration above PeV in the gamma-ray binaries require high resolution of MHD setups. Tracing the particle's energy change assumes that the simulated MHD quantities should be resolved on the scales smaller than particle's gyroradius R_g, while the sizes of the colliding flows regions of interest can reach tens AU. As for a proton with energy $\sim$0.1 PeV in the estimated $B \sim 1G$ the R_g is ~ 0.02 au, one is forced to use $\sim$1000 points per dimension to consider even minimal interesting dynamical range of sub-PeV particles. Studies of particle acceleration in a realistic model of binary's PWN flows assume scanning of the parameter space, that is very demanding to computational resources and forces to look for a some economical approach.

Bykov et al. [34] provided MHD-PIC simulations of PeV proton production in gamma-ray binaries in a planar 2D geometry and discussed the applicability of such model. They noted, that both the inflation of the PWN from the scratch and the acceleration of multi-PeV particles in such system occur on timescales below 10^5 s. This is much smaller than the orbital periods of known gamma-ray binaries [32, 33]. Moreover, it is even smaller than the expected timescale of pulsar's passage through orbital stage, where an efficient multi-PeV particles acceleration should be expected – e.g., the periastron region. Fast PWN inflation means that the structure of flows in region of winds' collision in gamma-ray binary quickly adjusts to the local conditions at the pulsar's orbit. Fast rate of acceleration and its localization in the close vicinity of the pulsar allows to consider only local structure of the winds' collision zone without computationally expensive simulation of its evolution along the pulsar's orbit.

Such simulation on a time interval short compared with the orbital timescales allows further simplification of the problem. If the PWN produced by the pulsar is small compared with the distance between

the stars, one may consider the upcoming SW as a uniform flow with fixed directions of uniform velocity and magnetic field. Moreover, in highly magnetized SW the local velocity tends to be aligned with the magnetic field. Thus, reasonable setup for studies of PeV particle acceleration in gamma-ray binaries reduces to a PWN inflating in a uniform magnetized flow with aligned magnetic field and velocity, whose magnitudes, as well as the pressure and mass density, are prescribed by known SW models. Bykov et al. [34] stated, that multi-PeV particle acceleration is not sensitive to the system's symmetry: crucial role is played only by the spatial scale of the acceleration site and spectrum of the magnetic inhomogeneities upscattering the particles. Keeping this in mind, they performed a planar 2D modeling. Here we simulate and analyse the flows structure in 2D and 3D and discuss the validity of planar models.

2. MODELING RESULTS

2.1. Structure of PWN in Strongly Magnetized Flow in 2D and 3D

The specific feature of discussed simulations is a high magnetization of the SW. To compare the 2D and 3D results we performed two sets of models for different possible SW magnetic field B_{sw}, listed in Table 1. The simulated PWN structure resulting from the interaction with a magnetized outflow of a massive star is shown in Fig. 1. It forms in a few hours for any of the studied system parameters. In the left column of Fig. 1 we show the map of the magnetic field after $t \approx 15$ h of PWN inflation in the 2D model. In the center and right columns the results of 3D simulations after $t \approx 2$ h are presented. These columns show the cross-sections of simulation box by two perpendicular planes: *XY*-plane, that contains the pulsar spin axis – *Y*-axis – and the $\mathbf{B}_{sw}$ direction, indicated by white arrows (middle column), and the equatorial *XZ*-plane (right column). Figure 1 illustrates the effect of the strong B_{sw} on the structure of PWN bubble. Rows correspond to $B_{sw} = 0.5, 1.0, 2.0$, and 3.0 G. Figure 2 illustrates the temporal evolution of the PWN for 3D setup with $B_{sw} = 2.0$ G and shows that at $t \approx 2$ h the PWNe seem to be already fully developed and expand almost self-similarly.

The structure of magnetized flows in 2D and 3D is qualitatively similar and shows similar details typical for rMHD models of the PWNe (e.g. [35–40]). In the center of the bubble one can see the region of cold relativistic wind, which is rapidly slowed down and heated up at the ∞-shaped TS (see Fig. 2 for velocity and pressure maps). The TS shape is typical for the rMHD models of PWNe and stems from the character of PW's anisotropy [41]. The PWN equator is occupied by a fast, turbulent, strongly magnetized outflow. Such an outflow is known to create an X-ray torus (or a double torus) in subsonic or slightly supersonic nebulae (like Crab and Vela). For isolated pulsars (like Crab and Vela), the torus rests at the equator of the nebula. In gamma-ray binaries, it may be tilted toward this equator. This is because the equatorial outflow tends to bend in different directions from the equator on the leeward and windward sides of the nebula. In our model, the outflow is rich in inhomogeneities of different spatial scales, which is also typical for PWN models in the literature, e.g., [37, 39]. These inhomogeneities can move with $v \sim 0.5c$ and even faster. The rest of the bubble's volume is occupied by the turbulized magnetized plasma full of slowly moving inhomogeneities. Finally, both in 2D and 3D the bubble is bordered by a magnetic cocoon produced from the SW's matter perturbed by the bubble's expansion.

Both in 2D and 3D with growth of B_{sw} the PWN bubble is narrowed across the external field and stretched along it. Along the field the PWN size is defined by the balance of the PW ram pressure with the pressure of SW matter, across the field the PW ram pressure can be compensated by the magnetic field tension. Simulations with the same B_{sw} in 2D and 3D are compared in each row of Fig. 1. The simulated maps in 2D (left column) and 3D (middle column) show a similar shape of the PWN bubbles – especially for strong fields ~2–3 G – despite of *very* different parameters of the PW, density and pressure of the SW (see Table 1). At lower fields the shape of the PWN's bubble is governed by two sources of anisotropy – the latitudinal PW's anisotropy, and the SW's magnetic field. The PW's energy flux has maximum at the equator providing elongation of the PWN's bubble in the equatorial plane. With growth of the B_{sw} the effect of the magnetic tension becomes stronger. A simple estimate of sufficient B_{sw} is given by comparison of the momentum density flux Φ, carried by the PWN plasma flow that expands with velocity u_{pw}, with the ambient magnetic pressure in the SW. If the magnetic pressure $B_{sw}^2/8\pi$ becomes comparable with $\Phi = \dot{E}/4\pi r^2 u_{pw}$ at distance r from the pulsar, then the PWN with size ~r would stretch along the B_{sw} direction. Then for the magnitude of $\mathbf{B}_{sw}$ one can write:

$$B_{sw} = \left(\frac{2\dot{E}}{u_{pw} r^2}\right)^{1/2} = 0.5\dot{E}_{37}^{1/2}\left(\frac{u_{pw}}{0.1c}\right)^{-1/2}\left(\frac{r}{10\,\mathrm{au}}\right)^{-1}\mathrm{G}.$$

Table 1. Parameters of the simulations. *SW*: $\mathbf{B}_{sw}$ – magnetic field in gauss, ψ is the angle between $\mathbf{B}_{sw}$ and pulsar's spin axis, n_{sw} and p_{sw} are the number density and pressure in cgs units. *PW*: $\dot{E}$ – pulsar's spindown luminosity in erg s^{-1}, α – the angle between the rotational and magnetic axes of the pulsar, σ_0 is the (initial) magnetization before annihilation of the stripes of the opposite polarities, Γ_w is the wind's Lorentz-factor. *Simulation domain:* "box" is the spatial dimensions of the whole domain, "core" – of the central region with uniform grid ($x_1 < x < x_2$, $y_1 < y < y_2$, and $z_1 < z < z_2$). r_{in} – radius of a small area from where the PW is continuously injected. N_x, N_y, N_z – the numbers of cells in x, y, and z coordinates. In 3D setups grids along y and z axes are identical. Setups with a uniform grid: *one* number is given in columns with N_x and N_y, N_z (central region occupies the entire domain). Setups with a patchy grid – with a uniform grid for $x_1 < x < x_2$ and grids with logarithmically growing step for $x > x_2$ and $x < x_1$ (the same for y and z dimensions): *three* numbers are given. The first and last give number of cells of the logarithmical grid at the axis ends, and the second – of the central uniform grid. Δ – grid resolution in the central region. The SW's velocity (as seen in the pulsar's coordinate system) is 300 km s^{-1} in all setups (see, e.g. [56])

Run	B_{sw}	ψ, deg	n_{sw}	p_{sw}	$\dot{E}$	α, deg	σ_0	Γ_w	Box, au^2/au^3	Core, au^2/au^3	r_{in}, au	N_x	N_y; N_z	Δ, au
A1	0.5	75	3×10^4	10^{-7}	10^{37}	45	3	100	40×40	40×40	0.15	1600	1600	0.025
A2	1	75	3×10^4	10^{-7}	10^{37}	45	3	100	40×40	40×40	0.15	1600	1600	0.025
A3	2	75	3×10^4	10^{-7}	10^{37}	45	3	100	40×40	40×40	0.15	1600	1600	0.025
A4	3	75	3×10^4	10^{-7}	10^{37}	45	3	100	40×40	40×40	0.15	1600	1600	0.025
A5	3	45	3×10^4	10^{-7}	10^{37}	45	0.3	100	40×40	40×40	0.15	1600	1600	0.025
A6	3	45	3×10^4	10^{-7}	10^{37}	80	3	100	40×40	40×40	0.15	1600	1600	0.025
X1	0.5	75	2×10^5	10^{-4}	10^{35}	80	0.3	4	$2\times1.46\times1.46$	$0.6\times0.6\times0.6$	0.02	340 + 600 + 340	252 + 600 + 252	0.001
X2	1	75	2×10^5	10^{-4}	10^{35}	80	0.3	4	$2\times1.46\times1.46$	$0.6\times0.6\times0.6$	0.02	340 + 600 + 340	252 + 600 + 252	0.001
X3	2	75	2×10^5	10^{-4}	10^{35}	80	0.3	4	$2\times1.46\times1.46$	$0.6\times0.6\times0.6$	0.02	340 + 600 + 340	252 + 600 + 252	0.001
X4	3	75	2×10^5	10^{-4}	10^{35}	80	0.3	4	$2\times1.46\times1.46$	$0.6\times0.6\times0.6$	0.02	340 + 600 + 340	252 + 600 + 252	0.001
X5	0.5	45	2×10^6	10^{-3}	10^{37}	80	0.3	4	$3\times3\times3$	$0.6\times0.6\times0.6$	0.027	363 + 451 + 363	363 + 451 + 363	0.0013
X6	0.5	75	2×10^5	2×10^{-4}	10^{35}	60	0.1	4	$2\times2\times2$	$0.6\times0.6\times0.6$	0.03	240 + 400 + 240	240 + 400 + 240	0.0015

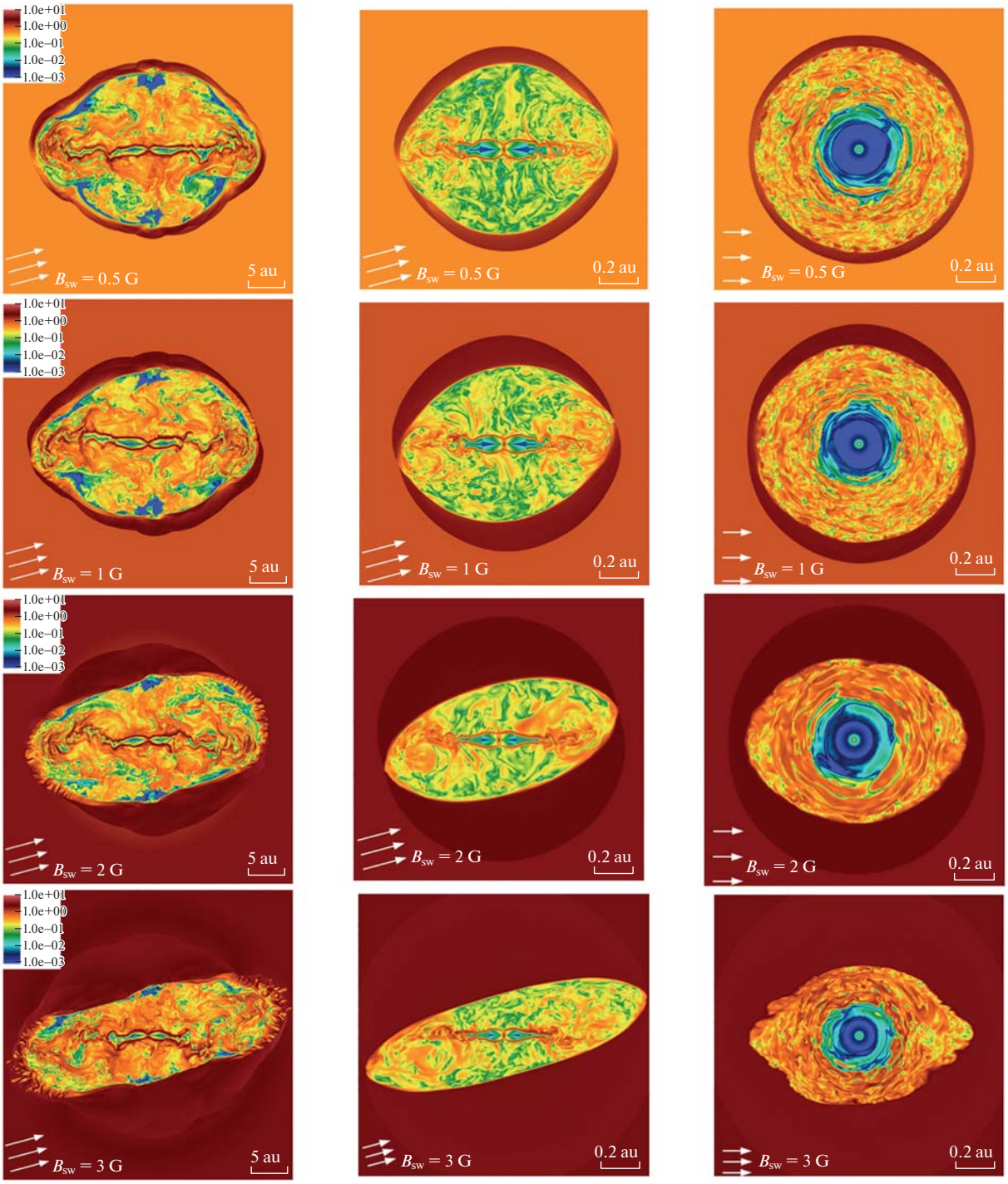

Fig. 1. Simulated maps of the colliding winds region for various magnitudes of the SW magnetic field. From top to bottom: results for B_{sw} = 0.5, 1, 2, and 3 G (for 2D models A1–A4 and 3D models X1–X4 in Table 1). The maps show the magnitude of the local B [G]. Left column – 2D simulations after $t \approx 15$ h of PWN inflation. Middle column – maps of the cross-section of the 3D simulation box by plane XY, and right – XZ – at $t \approx 2$ h (axis Y correspond to the pulsar spin axis). The SW magnetic field is directed under $\psi = 75°$ to Y-axis and is perpendicular to Z-axis. Note that the brightness scale of the color bar (universal for all panels) is adjusted to highlight the structure of MHD flows and does not reflect exactly the maximum and minimum values of B.

Thus, for $B_{sw} \sim 1$ G one can expect the elongated shape of the PWN even for very high $\dot{E} \sim 10^{37}$ erg s^{-1}. This is indeed what is observed both in 2D and 3D simulations, where the PWN's bubble becomes elon-

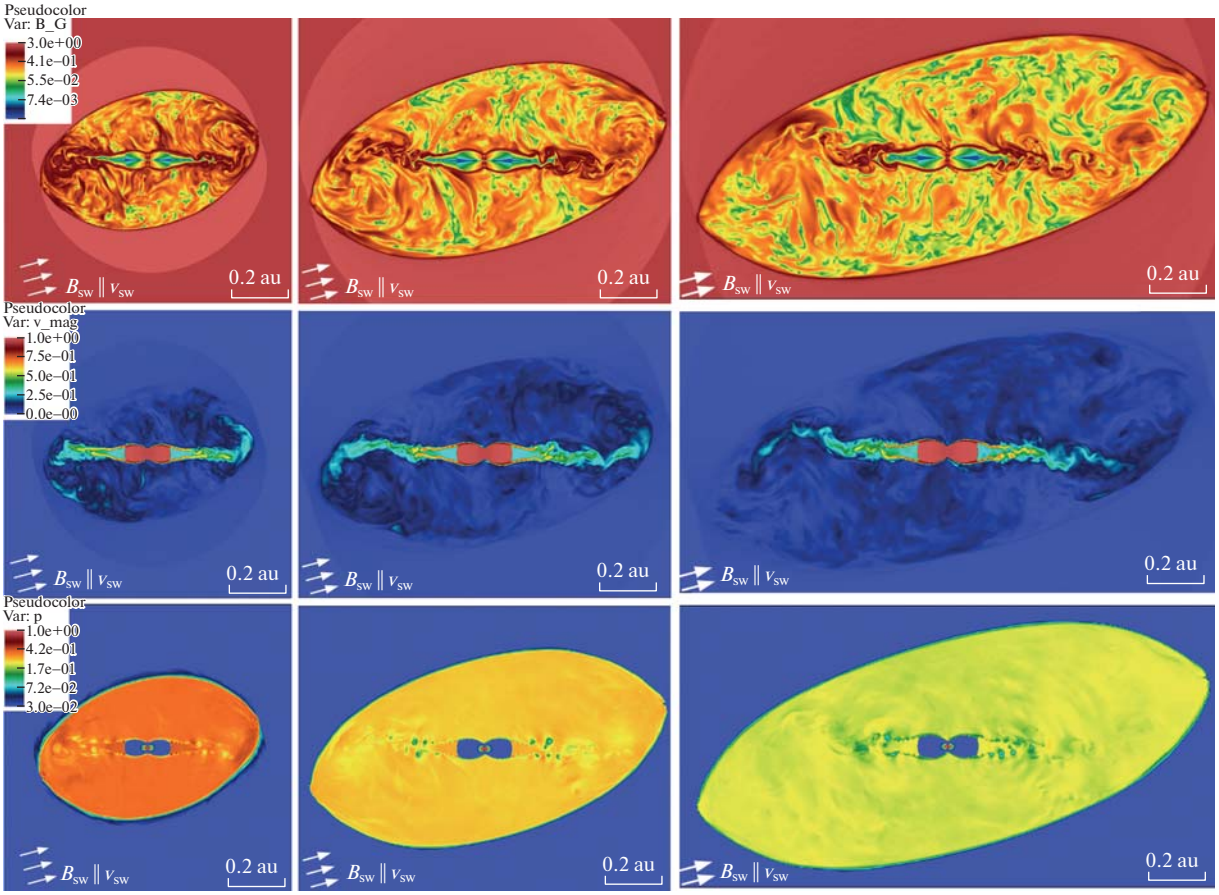

Fig. 2. Temporal evolution of the binary's PWN magnetic field (in G, top row), velocity (in units of c, middle row) and pressure (in cgs units, bottom row) for model X3 (Table 1). Shown are the cross-sections of 3D model by the plane containing pulsar's spin axis and SW magnetic field direction. Panels correspond to $t \approx 0.8$, 2, and 3 h since the simulation (PWN inflation) beginning. The brightness scale of the color bar (universal in each row) is adjusted to highlight the PWN structure and does not reflect exactly the maximum and minimum values of B, v/c, and p.

gated along the SW magnetic field for $B_{sw} \sim 2$–3 G. Ratio of the longitudinal to the transverse size of the bubble is similar for a fixed B_{sw} in 2D and 3D: it is about 0.5 for 2 G, and ≈0.3–0.35 for 3 G.

Another important feature observed both in 2D and 3D is production of dense magnetized cocoon around the PWN. In our setups the PWNe evolve inside a homogeneous flow of the SW with a uniform magnetic field. The expansion of the PWN bubble perturbs this flow, producing around the PWN bubble a zone of irregularized and amplified magnetic field. The plasma in this cocoon is a compressed SW plasma, that can be several times denser than in the surrounding SW – so, the magnetic field in the cocoon can be also several times stronger than B_{sw}. Interestingly, both in 2D and 3D the thickness of the cocoon tends to grow with B_{sw}.

Although the 2D and 3D results have much in common, we also found some differences. For the same PW parameters, the 3D PWNe look more stable and less turbulized. Comparison of our 2D and 3D simulations for pulsar inclination $\alpha = 80°$ (the tilt angle between pulsar's spin and magnetic axes) shows, that in 3D the TS front and the contact discontinuity (CD) between two winds are more stable and keep smoother shape, and the dynamics of the equatorial flows is less intense. These findings are consistent with results of pioneering 3D simulations of Porth et al. [38]. Third degree of freedom likely can destroy the enhanced coherence of the PWN flows and thus alleviate their impact on the TS structure. The 3D simulations also show noticeable dependence of the PWN's level of turbulence on α.

Despite of strong variability of shape and extension of the TS in 2D simulation, its size seems to be weakly dependent on the SW magnetic field. In contrary, size of 3D TS significantly decreases with the growth of B_{sw}. This is compatible with a standard estimate of spatial scale of termination/bow shock – the

standoff distance – the distance where the momentum flux produced by the pulsar's spin-down power is balanced by the external pressure. In case of the bow shock PWNe it is the upcoming flow's ram pressure ρu^2, whereas in the gamma-ray binaries one should consider $\rho u^2 + B_{sw}^2/8\pi$.

However, the general structure of the nebula in the 2D and 3D models is quite similar. This is remarkable because the compared models are created under different assumptions about the PW parameters and stellar wind parameters apart of its magnetic fields. In the following we consider in details the mildly-relativistic structures in the gamma-ray binaries that are of topical interest for problems of PeV particles acceleration in these objects.

2.2. Relativistic Flow Structures in Gamma-ray Binaries

The most prominent feature observed in Figs. 1, 2 is the equatorial strongly magnetized disk-like outflow, that harbors mildly relativistic flows. Its structure is similar to ones from the known rMHD models of PWNe in the literature. It consists of two highly-magnetized narrow-channel flows of opposite polarity, separated by a low-magnetized equatorial channel.

The highly- and low-magnetized flows originate from different sections of the ∞-shaped TS. The PW's energy flux latitudinal anisotropy can be described as $\propto \sin^2\theta$ [42]. Such flux has maximum at the equator $\theta = \pi/2$ and minimums at poles $\theta = 0$ and π. At poles the TS front approaches close to the pulsar, forming funnels, whereas at the equator it is at the greatest distance. In the equatorial section of the shock – the Mach belt – the wind outflow is normal to the shock and weakly magnetized. The low magnetization results from the annihilation of stripes with magnetic field of opposite polarity in the PW's equatorial sector (see Appendix A). At the Mach belt the normal flow of PW is efficiently decelerated. At higher latitudes, where the TS forms arched vaults, the strongly magnetized outflow experiences an oblique fall at the front. There deceleration is much less efficient, the outflow is slowed down at a complex of surfaces – the ached vaults of the TS front, the rim shock and the fast magnetosonic surface (see [36]) and still remains much faster than the equatorial flow. At the TS the highly magnetized flows are slowed down to $v/c \sim 0.8$–0.9 (Lorentz-factor $\Gamma \sim 2$), whereas finally they are terminated down to still supersonic $v \sim (0.6 - 0.7)c$.

The fast channels do not meet right after the TS, as typically occurs in the models of the PWN in a radially expanding supernova remnant (SNR) (e.g. [36, 38, 39]). They remain detached up to distance $\sim 2-3$ TS radii from the pulsar, like in models with PWN inflation in a free external flow [40, 43]. In the presence of an external flow, the pattern of nebular outflows and the TS geometry become more regular. In particular, the low-magnetized equatorial channel, entering the nebula in a strongly overcompressed state relative to its surroundings, can maintain its excess pressure and resist the intrusion of the neighbouring highly-magnetized channels at a large distance from the TS. Interestingly, it can harbor pressure pulsations (see Fig. 2) – alternating oblique and normal shocks – like a collimated outflow in a jet engine, that can influence on the dynamics of the fast highly magnetized outflows enveloping it.

At some distance from the TS depending on the pressure in the equatorial flow, the highly magnetized channels meet, mix and intertwine, producing an equatorial magnetized disk abundant with fast magnetic inhomogeneities interesting for particle acceleration. Both in 2D and 3D modeling the spacial extent of the fast magnetized outflows changes little with an increase in the external field by a factor of ~ 6 (Fig. 1). This suggests that the dynamical pressure of the outflows is quite comparable with the magnetic tension in the wind and with the ram pressure exerted by the wind on the orbiting nebula. Because of this, the PWN's volume occupied by highly magnetized outflows remains practically unchanged, despite the reduction in the total PWN volume. Along with the growth of the magnetic cocoon of the PWN with increasing B_{sw} it makes the gamma-ray binaries with higher B_{sw} more efficient particle accelerators, that was already shown by [34] for planar models.

2.3. Relativistic Clumps

In their 2D simulations of gamma-ray binaries, Bykov et al. [34] pointed to unusual structures: particularly fast-moving magnetic inhomogeneities ("relativistic clumps") with Lorentz factors $\Gamma \gtrsim 3$ and sub-AU sizes, which appear in the equatorial outflow of the nebula. Such clumps are of great importance for Fermi-type particle acceleration to energies above PeV. Accelerating particles gain energy in head-on collisions with magnetic inhomogeneities in turbulent flows. In a single head-on collision, a particle can boost its energy by a factor of Γ^2, i.e., by the squared Lorentz factor of the encountered inhomogeneity.

For the energy gain to be so significant, the inhomogeneity must be comparable in size to the particle's gyroradius. The sub-AU scales of the relativistic clumps allow them to effectively upscatter pre-accelerated sub-PeV particles, since the latter have gyroradii $\lesssim 1$ au in the Gauss-range magnetic fields typical of PWNe in gamma-ray binaries. For the clumps, the factor Γ^2 is almost an order of magnitude as large as that for the usual magnetic inhomogeneities. Therefore, the clumps are much more efficient and can turn a sub-PeV particle into a PeV one in just a few successful scatterings.

The nature of the relativistic clumps remains to be elucidated, since they seem to form differently and have higher Lorentz factors than the usual large-scale magnetic inhomogeneities. The latter typically arise at the rims of the termination shock in the form of magnetic eddies, generated by strong distortions of the shock's working surface[1] [37, 38]. The eddies are then launched into the nebula and advected outward with its turbulent equatorial flow. Their Lorentz factors Γ can be assessed from observations of the Crab Nebula and from rMHD simulations of PWNe. In Crab they are seen in radio, optical, and X-rays as fine, prominently bright arc-shaped synchrotron features. They originate at the wind termination shock and propagate outward with $v/c \sim 0.5$–0.6, corresponding to $\Gamma \sim 1.2$ [44]. Similar Lorentz factors are demonstrated by large-scale eddies in the equatorial flows in rMHD models[2] of Crab-like nebulae, objects with a single-torus morphology in X-rays. A characteristic feature of these objects is that flows of opposite magnetic polarities, arising in different hemispheres of the nebula, meet and intertwine immediately after the rim of the shock, thereby giving rise to a turbulent equatorial flow. Meanwhile, the relativistic clumps appear to originate not at the shock, but at some distance from it. They certainly correlate with strong depressions that occur on either side of the wide, overcompressed, weakly-magnetized equatorial flow, where it temporally collapses or narrows greatly. Such a flow is characteristic of another class of PWNe, the prototype of which is the Vela PWN, an object with a double-torus X-ray morphology. In these objects, the flows of opposite polarity, running on either side of the overcompressed equatorial flow, remain strongly magnetized, quasi-laminar and ultrarelativistic. Their typical Lorentz factors can come to $\Gamma \sim 1.5$–1.9 (i.e., $v/c \sim 0.7$–0.85).

The role of relativistic clumps in particle re-acceleration can be illustrated using a simple Monte-Carlo model. In it, a clump is modeled as a subregion embedded in the region of the pulsar wind, which in turn collides with the stellar wind. The embedded subregion has a sub-AU size and a high-speed flow with a certain Γ. A population of pre-accelerated particles is then injected in the system and allowed to interact with it (see details in Appendix B). The result is presented in Fig. 3 on the left panel. There, several spectral energy distributions are shown in color: in red – for particles just injected in the system, in orange – for those that were accelerated only in colliding flows, and in green, blue, and purple – for those that were accelerated in colliding flows with the clump. (The last three spectra differ in the clump's Lorentz factor, which is $\Gamma = 3, 4.5$, and 6, respectively). It can be seen that the acceleration in the colliding flows alone makes the spectral distribution much harder, with a single hump at sub-PeV energies. Embedding a clump with $\Gamma \gtrsim 3$ in the colliding flows results in a double-humped spectrum with a second hump at energies well above PeV.

According to our 2D simulations, the clumps can arise in PWNe with very different parameters (see Fig. 4). The clumps with $\Gamma \gtrsim 3$ can be more than 1 AU in size, i.e., larger, than the gyroradius of 10 PeV particles in a 1 G field. These clumps can persist in turbulent flows of the nebula for a few hours (Fig. 4), which is more than enough time for re-acceleration to occur [34].

In agreement with the result of Porth et al. [38], in 3D nebulae the termination shock is less dynamic and magnetic turbulence is less intense. Nevertheless, particularly fast-moving magnetic clumps still arise in the nebula, just as in 2D models, but smaller in size and with lower Γ. This can be seen in Fig. 5, in the bottom two rows. In models with $\alpha = 80°$ they have $\Gamma \gtrsim 2$ and sizes of several percents of AU in the meridional plane (where the pulsar's spin axis lies) and several tenths of AU in the plane parallel to the equatorial plane of the nebula (Fig. 6). Whether this decrease in size and speed of the clump is a feature of 3D nebulae or a consequence of the insufficiently high resolution of 3D models (see below) remains to be seen. In any case, 3D clumps are larger, faster and more numerous, the more strongly the pulsar wind is magnetized.

[1] Note that modern relativistic MHD models of PWNe are built on a simplified prescription for the pulsar wind, in which the wind itself is uniform (in terms of density).

[2] This estimate applies to flows that have already been thrown into the nebula from the arched vaults of the wind's termination shock. For flows still running along these vaults, a velocity estimate can be found in [45]. Note that the latter flows are very narrow and quasi-laminar and therefore cannot upscatter PeV-regime particle, no matter how high their Γ is. They can only help to confine such a particle in the accelerator.

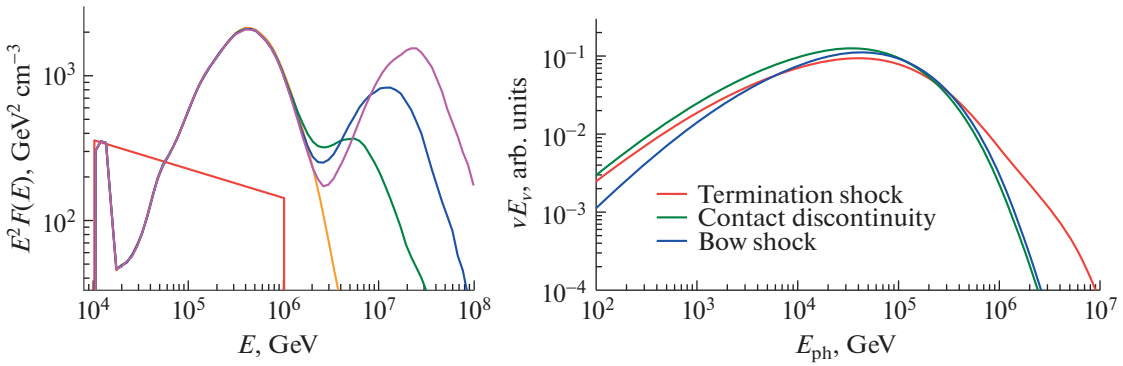

Fig. 3. Left: Particle acceleration in gamma-ray binaries: results of Monte Carlo simulations. Several spectral energy distribution are shown in color: in red – for the particles that have just been injected in the system, in orange – for those that were accelerated in the colliding flows alone, and in green, blue, and purple – for those that were accelerated in the colliding flows with the relativistic clump. The last three spectra differ in the clump's Lorentz factor, which is $\Gamma = 3$, 4.5, and 6, respectively. Right: simulated synchrotron spectra of the Vela PWN. Spectra of different colors are obtained by integration of the simulated synchrotron emissivity integrating over different lines of sight (l.o.s.). Red – l.o.s. coming close to the TS, blue – to the bow shock, green – to the contact discontinuity. Spectra of radiating particles in the entire volume of the model PWN were obtained in Monte Carlo simulations.

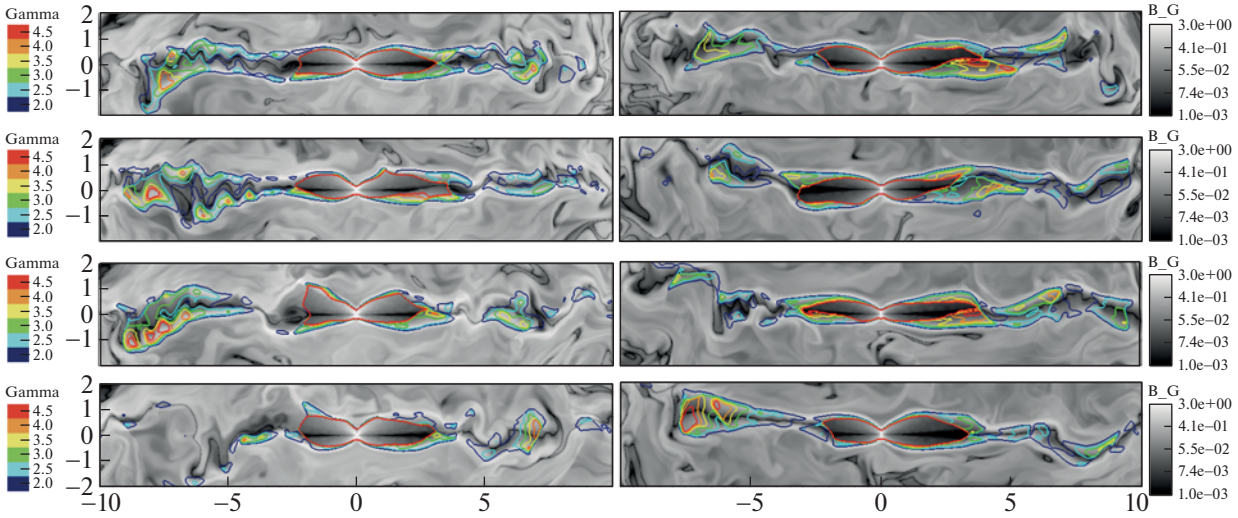

Fig. 4. Relativistic clumps in pulsar wind nebulae. Shown are two 2D models A5 and A6 in Table 1: $\alpha = 45°$, $\sigma_0 = 0.3$ (left column) and $\alpha = 80°$, $\sigma_0 = 3$ (right column). Contour maps of the Lorentz-factor are superimposed onto gray colormaps of the magnetic field B (in G) given to guide the eye. Each row corresponds to a certain moment of time since the start of simulation; from top to bottom: $t = 11.1$, 11.8, 12.5, and 13.2 h. Brightness scale of the gray color bar is adjusted to highlight the structure of rMHD outflows and does not reflect the maximum and minimum values of B. Note that the contour $\Gamma_w = 4.5$, that outlines the region of the unshocked pulsar wind, almost coincides with the position of the wind termination shock, due to the abrupt deceleration of the wind.

Relativistic clumps appear over a wide range of grid resolutions and over a large region of parameter space. As expected, their sizes and Lorentz factors depend on resolution of the numerical grid.[3] This is illustrated in Fig. 6 for a number of 2D setups. This is a standard situation in modeling within the ideal rMHD approach, in which artificial numerical viscosity (determined by grid's resolution) replaces the real plasma viscosity.

[3] They also depend on the convergence of the numerical scheme on which the numerical code is based; examples in the field of PWNe modeling can be found, e.g., in [38].

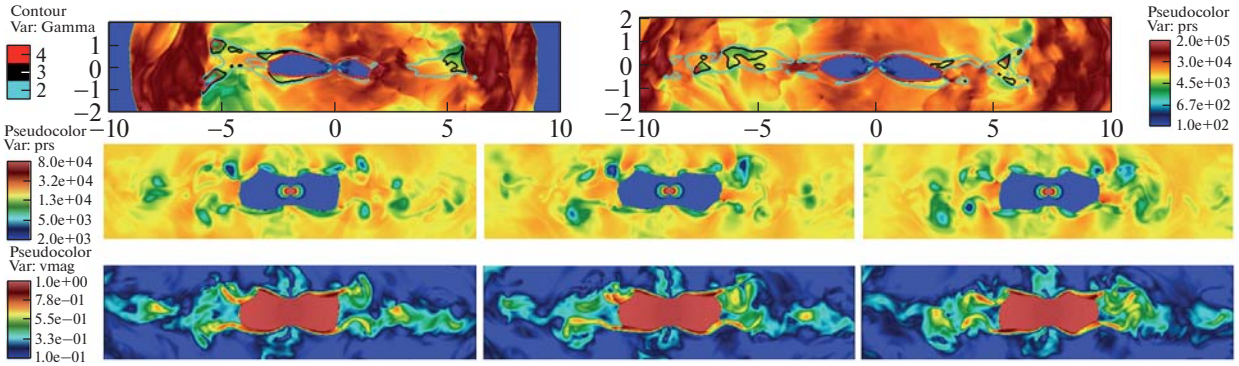

Fig. 5. Relativistic clumps in pulsar wind nebulae: 2D vs 3D rMHD simulations of colliding winds in gamma-ray binaries. Enlarged images of the equatorial region of the nebula. Top row (2D case): Two pressure colormaps with superimposed contour maps of the flow Lorentz factors $\Gamma > 2$. Two images of the nebula were taken at times $t \approx 7.6$ and 9.7 h after the start of the simulation based on model A5 in Table 1 (with $\alpha = 45°$, $\sigma_0 = 0.3$). Pressure's colorbar is in units of $p_0 = 9 \times 10^{-6}$ dyn cm^{-2}. Bottom two rows (3D case): Correlation of depressions and clumps with a high Lorentz factor. Shown are colormaps of pressure (in units of p_0; top row) and flow velocity (in units of c; bottom row). The columns correspond to three consecutive snapshots of the nebula taken at time $t \approx 1.3$ hour from the start of the simulation with a time step of ~ 100 s. The simulation is based on model X6 in Table 1 (with $\alpha = 60°$, $\sigma_0 = 0.1$). The brightness scales of the colorbars are adjusted to highlight the structure of outflows and do not reflect the maximum and minimum values of the quantities.

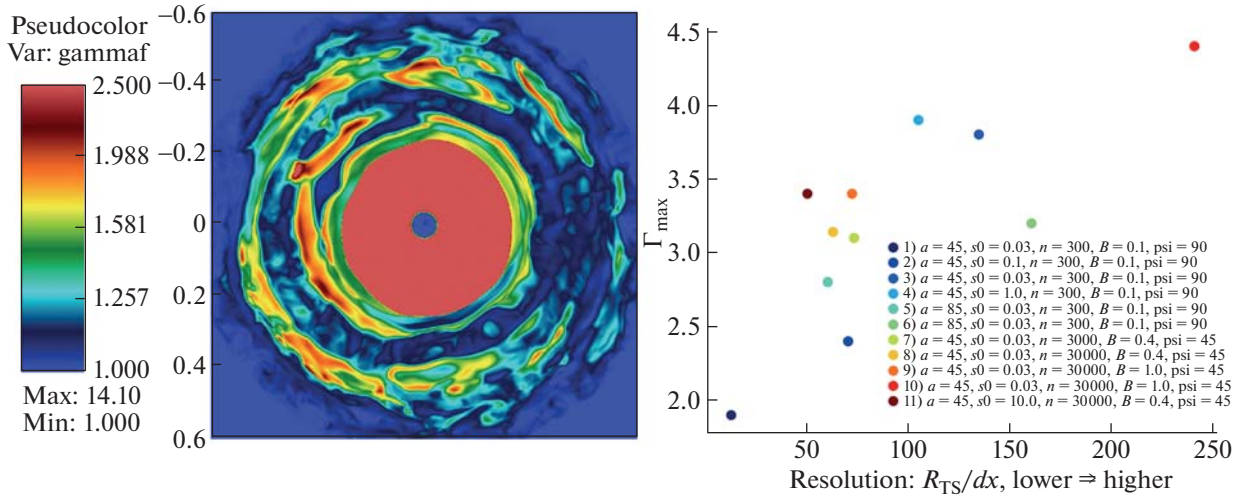

Fig. 6. Left: Simulated color map of the Lorentz-factor Γ of nebular flows (model X5 in Table 1). Shown is a cross-section of the 3D nebula by a plane parallel to its equatorial plane and offset from it by 0.058 au. The brightness scale of the color bar is adjusted to highlight the structure of rMHD flows and does not reflect the maximum and minimum values of Γ. Right: Maximum Lorentz factor of relativistic clumps as a function of numerical grid resolution, for different 2D rMHD setups. The resolution is parameterized by the number of grid's nodes within the equatorial radius R_{TS} of the termination shock.

2.4. Astrospheres of Isolated Pulsars. The Vela Nebula

Like PWNe in gamma-ray binaries, isolated nebulae can also be affected by a strong external flow. An example is the Vela Nebula. Its slow-moving pulsar encounters a fast counter-flow initiated by the passage (over the nebula) of the reverse shock of the supernova [46]. This counter-flow turns out to be weakly supersonic in the pulsar's reference frame. Accounting for this supersonic flow is necessary for interpreting all synchrotron features of Vela's X-ray morphology, from its complexly structured asymmetric jets to its enigmatic double-torus[4] [40, 43, 48]. The strong external flow also helps in interpreting the reverbera-

[4] Similarly, accounting for the strong external flow caused by an asymmetric expansion of a supernova remnant is important for interpreting the "inner ring" synchrotron feature and the asymmetric jets in the Crab Nebula [47].

tions of the double-torus and its precession as a whole [49]. Taking this flow in account is also required for spectral modeling of the Vela Nebula. Its hard X-ray photon indexes can be understood in a model of the collision of a pulsar wind with a weakly supersonic ejecta flow. This was shown in Monte Carlo simulations of particle acceleration in collision of such flows [50].

Interestingly, this model predicts a significant flux of synchrotron radiation from Vela in the MeV range. In the right panel of Fig. 3 we show the simulated spatially resolved synchrotron spectra of Vela. They were obtained by integration along a bunch of lines of sight of the simulated synchrotron emissivity, that was calculated in the cells of 3D grid permeating the model PWN volume. In each of those cells the model particle spectrum was simulated in the Monte Carlo modeling. Red curve shows the spectrum for a line of sight coming close to the TS, blue – close to the bow shock produced in interaction with the upcoming flow, green – through the region where these flows are separated by a CD. Interestingly, the model predicts the MeV flux only a few times lower than the X-ray flux detected by Chandra.

A potentially detectable MeV flux is likely a common feature of astrospheres of pulsars and gamma-ray binaries whose flows are powerful enough to produce PeV-range charged particles. The Vela pulsar can accelerate sub-PeV particles due to its high spin-down (i.e., wind) power $\dot{E} \approx 7\times10^{36}$ erg s^{-1}, while pulsars in binaries – even with lower spin-down power – due to the strong magnetic field in the powerful stellar wind of the massive companion.

3. CONCLUSIONS

We discussed above the results of relativistic MHD simulations of the structure of PWNe produced in collision of the relativistic pulsar wind and strongly magnetized wind of a young massive star in the gamma-ray binaries. The distinctive feature of these simulations is account for the effects of a strong Gauss-range SW magnetic field B_{sw} available at the distances of a few astronomical units from the star. The presence of strong B_{sw} results in the globally elongated shape of the pulsar wind nebula both in 2D and 3D. Similar elongated bubbles were obtained recently by Meyer et al. [51] in the non-relativistic 2D MHD simulations of plerionic type supernova remnants in the magnetized circumstellar medium. Our simulations show that the global structures of flows in 2D and 3D are very similar. Also, most of the morphological features that were earlier found by Bykov et al. [34] in planar morphology are well reproduced in much more computationally demanding 3D simulations presented here. This agrees with the conclusions of Bosch-Ramon et al. [26], who studied the effects of the orbital motion on the binary structure in relativistic HD without strong magnetic fields and found their 2D and 3D results qualitatively very similar.

At smaller scales the mildly relativistic MHD flows in the region of the collision of the pulsar wind with the strongly magnetized massive star wind facilitates relativistic proton acceleration to PeV regime at a short part of the binary period. The relativistic clumps of scales comparable or larger than the gyroradii of PeV regime protons obtained in the RMHD simulations of gamma-ray binaries are very important for studies of potential pevatrons. These structures may allow the young pulsars interacting with highly magnetized wind of the binary companion star to accelerate protons well above the limit defined by the magnetospheric potential. Simulations with higher numerical resolution are important to study the limits of possible Lorentz-factor and size of relativistic clumps.

APPENDIX A

rMHD Modeling Setups

Our rMHD simulations of gamma-ray binaries are based on Relativistic MHD module of the code PLUTO [52]. In this study, we examine the local structure of the region where the winds of the binary companions collide. This region encompasses a pulsar wind nebula (PWN), and a dense cocoon that is formed around it from the matter of the wind of the pulsar's massive companion (here, a Be-type star). According to arguing in section 1, the wind of the massive companion is initialized as a homogeneous, strongly magnetized flow with co-directional magnetic field and velocity. The wind's parameters are given in Table 1. They are chosen to illustrate the variety of conditions in the stellar wind that the pulsar might encounter where its orbit takes it close to the Be star. Note, however, that the local structure of the PWN depends weakly on the velocity and density of the stellar wind, as long as the latter is strongly magnetized.

To inflate the pulsar wind nebula, we apply a simplified model of the pulsar wind which is widely used in modern rMHD simulations of isolated nebulae (e.g. [38–40]. In this model, the wind is cold and its

energy flux density is latitudinally dependent, with a maximum at the plane of the rotational equator of the pulsar (this plane determines the equatorial plane of the nebula):

$$f_{\rm tot}(r,\theta) = \frac{\dot{E}}{L_0}\frac{1}{r^2}\left(\sin^2\theta + \varepsilon\right).$$

Here r is a distance from the pulsar, θ is colatitude, $L_0 = 4\pi(2/3+\varepsilon)$ is normalization constant, $\varepsilon = 0.02$ prevents the flux from vanishing at the poles. The energy flux is divided into magnetic and kinetic components, $f_{\rm tot} = f_m + f_k$, the ratio of which is determined by the magnetization $\sigma = f_m/f_k$ of the cold pulsar wind upstream of the wind termination shock:

$$f_m(r,\theta) = \frac{\sigma(\theta) f_{\rm tot}(r,\theta)}{1+\sigma(\theta)}; \quad f_k(r,\theta) = \frac{f_{\rm tot}(r,\theta)}{1+\sigma(\theta)}; \quad \sigma(\theta) = \frac{\tilde{\sigma}(\theta)\chi_\alpha(\theta)}{1+\tilde{\sigma}(\theta)(1-\chi_\alpha(\theta))}.$$

Magnetic field of the wind is purely toroidal, frozen in the plasma and latitudinally dependent. It almost vanishes near the rotational equator and toward the poles and has a maximum at the middle latitudes. These features are accounted with the functions χ and $\tilde{\sigma}$:

$$\tilde{\sigma}(\theta) = \sigma_0 \cdot \min\left\{1, \frac{\theta^2}{\theta_0^2}, \frac{(\pi-\theta)^2}{\theta_0^2}\right\}; \quad \chi_\alpha(\theta) = \begin{cases} (2\phi_a(\theta)/\pi - 1)^2 & \text{if} \quad \left|\frac{\pi}{2} - \theta\right| < \alpha \\ 1 & \text{otherwise,} \end{cases}$$

with $\phi_\alpha(\theta) = \arccos(-\cot(\theta)\cot(\alpha))$ and a typical value of $\theta_0 = 10°$. Here σ_0 is the initial magnetization of the pulsar wind. Due to the facts that the field changes sign at the magnetic equator of the pulsar, that the magnetic and rotational equators makes an angle α to each other, and that the pulsar rotates, the magnetic field of the wind alternates at the equatorial latitudes of the nebula. In the result, the wind at these latitudes become striped: it carries the stripes of plasma of alternating magnetic polarity which fill the angular sector $\pm\alpha$. Either on their way to the TS, or due to their compression right at the shock, the stripes can annihilate [53–55], so the magnetic field in the equatorial sector $\pm\alpha$ dissipates almost completely. For the pulsar wind's density, magnetic field and velocity, we have:

$$\rho_{\rm pw}(r,\theta) = f_k(r,\theta)/\Gamma_w^2 c^3, \quad B_{\rm pw}(r,\theta) = \pm\sqrt{4\pi f_m(r,\theta)/c}, \quad u_{\rm pw}/c = \sqrt{1-\Gamma_w^{-2}}.$$

The wind is radially directed and has a Lorentz-factor Γ_w. In the simulation we use Cartesian 2D/3D grids. The pulsar's spin axis is aligned with Cartesian y-axis; $r = (x^2+y^2+z^2)^{1/2}$ and $\theta = \arccos(y/r)$, and $z = 0$ in 2D.

APPENDIX B

Simplified Anisotropic Monte Carlo Model

To simulate particle re-acceleration by relativistic clumps with $\Gamma > 2$ (which appear in rMHD models of pulsar wind nebulae in gamma-ray binaries), we developed a massively parallelized numerical code based on the Monte Carlo approach. The code is three-dimensional and implements the propagation of charged particles in a turbulent magnetic field with a strong regular component.

The computation domain is a cylinder with radius $R_{\rm box}$ and length $l_{\rm box} = 2R_{\rm box}$ and a uniform magnetic field $B_{\rm box}$ parallel to the cylinder's axis. Two colliding winds – pulsar and stellar – are modeled as two magnetized uniform flows, each of which occupies half of the cylinder. The winds' velocities – $\mathbf{u}_{\rm pw}$ and $\mathbf{u}_{\rm sw}$ – are counter-directed and parallel to the cylinder's axis. The contact discontinuity (CD) between the winds is represented by a narrow buffer region with zero flow velocity. The clump is modeled as a small cylindical subregion embedded in the region of the pulsar wind. The simulation parameters reproduce the conditions in gamma-ray binaries: $R_{\rm box} \approx 3$ au, $B_{\rm box} = 0.1$ G, $u_{\rm pw} = 0.57c$, and $u_{\rm sw} = 3\times10^4$ km s^{-1}. The clump has a size of 0.6×1.2 au and a flow velocity with a high Lorentz factor Γ. We considered the cases with $\Gamma = 3$, 4.5, and 6. The result of the Monte Carlo simulation is shown in Fig. 3, on the left panel.

The simulation of acceleration begins by injecting a population of non-thermal particles into the CD region. The injected population is assumed to be pre-accelerated (e.g., on the wind termination shock), having an initial spectrum $f_{\rm TS}(E) \propto E^{-2.2}$. The particles then move along their (helical) trajectories prescribed by Newtonian laws for a certain free-flight time $t_{\rm mfp}$. After that, each particle is scattered isotrop-

ically (in the rest frame of a local background flow), and moves again for time t_{mfp}, and so on, until it leaves the computational domain through its border with the free escape boundary conditions. The free-flight time t_{mfp} is determined by the mean free path $\lambda_{\mathrm{mfp}} = ct_{\mathrm{mfp}} = \eta R_g$, with $\eta \geq 3$ in the pulsar wind's, the stellar wind's and the CD regions, where R_g is the particle gyroradius.

FUNDING

Modeling of MeV radiation was performed by A.M.B. with computational facilities supported from the MON grant 075-15-2024-647. Monte Carlo simulations by A.E.P. were supported by the Foundation for the Advancement of Theoretical Physics and Mathematics "BASIS." Data analysis by K.P.L. was supported by the baseline project FFUG-2024-0002 at the Ioffe Institute. Some of the modeling was performed at the "Tornado" subsystem of the St. Petersburg Polytechnic University Supercomputing Center. We acknowledge Georgy Ponomaryov for his contribution to our numerical studies of PWNe and gamma-ray binaries.

CONFLICT OF INTEREST

The authors of this work declare that they have no conflicts of interest.

REFERENCES

1. Sobolev, V.V., *Moving Envelopes of Stars,* Harvard: Univ. Press, 1960.
2. Baranov, V.B. and Krasnobaev, K.V., *Gidrodinamicheskaya teoriya kosmicheskoi plazmy* (Hydrodynamic Theory of a Cosmic Plasma), Moscow: Nauka, 1977.
3. Lamers, H.J.G.L.M. and Cassinelli J.P., *Introduction to Stellar Winds,* Cambridge: Univ. Press, 1999.
4. ud-Doula, A., Owocki, S.P., Russell, C., Gagne, M., and Daley-Yates, S., 3D MHD models of the centrifugal magnetosphere from a massive star with an oblique dipole field, *Mon. Not. R. Astron. Soc.,* 2023, vol. 520, p. 3947.
5. Parker, E.N., *Interplanetary Dynamical Processes,* New York: Intersci. Publ., 1963.
6. Baranov, V.B., Krasnobaev, K.V., and Kulikovskii, A.G., A model of the interaction of the solar wind with the interstellar medium, *Sov. Phys. Dokl.,* 1971, vol. 15, p. 791.
7. Richardson, J.D., Bykov, A., Effenberger, F., Scherer, K., von Steiger, R., Sterken, V.J., and Zank, G.P., *The Heliosphere in the Local Interstellar Medium: into the Unknown,* Springer, 2023.
8. Godenko, E.A. and Izmodenov, V.V., Dynamical charging of interstellar dust particles in the heliosphere, *Adv. Space Res.,* 2023, vol. 72, p. 5142.
9. Hester, J.J., The Crab Nebula: an astrophysical chimera, *Annu. Rev. Astron. Astrophys.,* 2008, vol. 46, p. 127.
10. Fang, K., Bi, X.-J., and Yin, P.-F., Reanalysis of the pulsar scenario to explain the cosmic positron excess considering the recent developments, *Astrophys. J.,* 2019, vol. 884, p. 124.
11. Arons, J., Pulsar wind nebulae as cosmic pevatrons: a current Sheet's tale, *Space Sci. Rev.,* 2012, vol. 173, p. 341.
12. Dubus, G., Gamma-ray binaries: pulsars in disguise?, *Astron. Astrophys.,* 2006, vol. 456, p. 801.
13. Neronov, A. and Chernyakova, M., Radio-to-TeV γ-ray emission from PSR B1259–63, *Astrophys. Space Sci.,* 2007, vol. 309, p. 253.
14. Neronov, A. and Ribordy, M., Neutrino signal from γ-ray-loud binaries powered by high energy protons, *Phys. Rev. D,* 2009, vol. 79, p. 043013.
15. Bykov, A.M., Petrov, A.E., Kalyashova, M.E., and Troitsky, S.V., Neutrino signal from γ-rayloud binaries powered by high energy protons, *Astrophys. J.,* 2021, vol. 921, p. L10.
16. Dubus, G., Gamma-ray binaries and related systems, *Astron. Astrophys. Rev.,* 2013, vol. 21, p. 64.
17. Yoneda, H., Makishima, K., Enoto, T., Khangulyan, D., Matsumoto, T., and Takahashi, T., Sign of hard-X-ray pulsation from the γ-ray binary system LS 5039, *Phys. Rev. Lett.,* 2020, vol. 125, p. 111103.
18. Kargaltsev, O., Hare, J., Volkov, I., and Lange, A., A lack of 9 s periodicity in the follow-up NuSTAR observation of LS 5039, *Astrophys. J.,* 2023, vol. 958, p. 79.
19. Makishima, K., Uchida, N., Yoneda, H., Enoto, T., and Takahashi, T., Further evidence for the 9 s pulsation in LS 5039 from NuSTAR and ASCA, *Astrophys. J.,* 2023, vol. 959, p. 79.
20. Weng, S.-S., Qian, L., Wang, B.-J., Torres, D.F., Papitto, A., Jiang, P., Xu, R., Li, J., Yan, J.-Z., Liu, Q.-Z., Ge, M.-Y., and Yuan, Q.-R., Radio pulsations from a neutron star within the gamma-ray binary LS I +61° 303, *Nat. Astron.,* 2022, vol. 6, p. 698.
21. Lopez-Miralles, J., Motta, S.E., Migliari, S., and Jaron, F., Rapid X-ray variability of the gamma-ray binary LS I +61° 303, *Mon. Not. R. Astron. Soc.,* 2023, vol. 523, p. 4282.

22. Cao, Z., Aharonian, F.A., An, Q., Axikegu Bai, L.X., Bai, Y.X., Bao, Y.W., Bastieri, D., Bi, X.J., Bi, Y.J., Cai, H., Cai, J.T., Cao Zhe, Chang, J., Chang, J.F., Chang, X.C., et al., Ultrahigh-energy photons up to 1.4 petaelectronvolts from 12γ-ray Galactic sources, *Nature,* 2021, vol. 594, p. 33.
23. Dzhappuev, D.D., Afashokov, Y.Z., Dzaparova, I.M., Dzhatdoev, T.A., Gorbacheva, E.A., Karpikov, I.S., Khadzhiev, M.M., Klimenko, N.F., Kudzhaev, A.U., Kurenya, A.N., Lidvansky, A.S., Mikhailova, O.I., Petkov, V.B., Podlesnyi, E.I., Romanenko, V.S., Rubtsov, G.I., Troitsky, S.V., Unatlokov, I.B., Vaiman, I.A., Yanin, A.F., Zhezher, Ya.V., Zhuravleva, K.V., and Carpet-3 Group, Observation of photons above 300 TeV associated with a high-energy neutrino from the Cygnus region, *Astrophys. J.,* 2021, vol. 916, p. L22.
24. Bosch-Ramon, V. and Barkov, M.V., Large-scale flow dynamics and radiation in pulsar γ-ray binaries, *Astron. Astrophys.,* 2011, vol. 535, p. A20.
25. Bosch-Ramon, V., Barkov, M.V., Khangulyan, D., and Perucho, M., Simulations of stellar/pulsar-wind interaction along one full orbit, *Astron. Astrophys.,* 2012, vol. 544, p. A59.
26. Bosch-Ramon, V., Barkov, M.V., and Perucho, M., Orbital evolution of colliding star and pulsar winds in 2D and 3D: effects of dimensionality, EoS, resolution, and grid size, *Astron. Astrophys.,* 2015, vol. 577, p. A89.
27. Dubus, G., Lamberts, A., and Fromang, S., Modelling the high-energy emission from gammaray binaries using numerical relativistic hydrodynamics, *Astron. Astrophys.,* 2015, vol. 581, p. A27.
28. Bosch-Ramon, V., Barkov, M.V., Mignone, A., and Bordas, P., HESS J0632+057: hydrodynamics and nonthermal emission, *Mon. Not. R. Astron. Soc.,* 2017, vol. 471, p. L150.
29. Huber, D., Kissmann, R., and Reimer, O., Relativistic fluid modelling of gamma-ray binaries. II. Application to LS 5039, *Astron. Astrophys.,* 2021, vol. 649, p. A71.
30. Grunhut, J.H., Wade, G.A., Neiner, C., Oksala, M.E., Petit, V., Alecian, E., Bohlender, D.A., Bouret, J.C., Henrichs, H.F., Hussain, G.A.J., Kochukhov, O., and MiMeS Collab., The MiMeS survey of magnetism in massive stars: magnetic analysis of the O-type stars, *Mon. Not. R. Astron. Soc.,* 2017, vol. 465, p. 2432.
31. Shultz, M.E., Wade, G.A., Rivinius, T., Alecian, E., Neiner, C., Petit, V., Owocki, S., Doula, A., Kochukhov, O., Bohlender, D., Keszthelyi, Z., MiMeS Collab., and BinaMIcS Collab., The magnetic early B-type stars – III. A main-sequence magnetic, rotational, and magnetospheric biography, *Mon. Not. R. Astron. Soc.,* 2019, vol. 490, p. 274.
32. Casares, J., Ribo, M., Ribas, I., Paredes, J.M., Marti, J., and Herrero, A., *Mon. Not. R. Astron. Soc.,* 2005, vol. 364, p. 899.
33. Ho, W.C.G., Ng, C.Y., Lyne, A.G., Stappers, B.W., Coe, M.J., Halpern, J.P., Johnson, T.J., and Steele, I.A., A possible black hole in the γ-ray microquasar LS 5039, *Mon. Not. R. Astron. Soc.,* 2017, vol. 464, p. 1211.
34. Bykov, A.M., Petrov, A.E., Ponomaryov, G.A., Levenfish, K.P., and Falanga, M., PeV proton acceleration in gamma-ray binaries, *Adv. Space Res.,* 2024, vol. 74, no. 9, p. 4276.
35. Komissarov, S.S. and Lyubarsky, Y.E., Synchrotron nebulae created by anisotropic magnetized pulsar winds, *Mon. Not. R. Astron. Soc.,* 2004, vol. 349, p. 779.
36. Del Zanna, L., Amato, E., and Bucciantini, N., Axially symmetric relativistic MHD simulations of pulsar wind nebulae in supernova remnants. On the origin of torus and jet-like features, *Astron. Astrophys.,* 2004, vol. 421, p. 1063.
37. Camus, N.F., Komissarov, S.S., Bucciantini, N., and Hughes, P.A., Observations of "wisps" in magnetohydrodynamic simulations of the Crab nebula, *Mon. Not. R. Astron. Soc.,* 2009, vol. 400, p. 1241.
38. Porth, O., Komissarov, S.S., and Keppens, R., Three-dimensional magnetohydrodynamic simulations of the Crab nebula, *Mon. Not. R. Astron. Soc.,* 2014, vol. 438, p. 278.
39. Buhler, R. and Giomi, M., The imprint of pulsar parameters on the morphology of pulsar wind nebulae, *Mon. Not. R. Astron. Soc.,* 2016, vol. 462, p. 2762.
40. Ponomaryov, G.A., Fursov, A.N., Fateeva, S.S., Levenfish, K.P., Petrov, A.E., and Krassilchtchikov, A.M., On the origin of knots in the Vela nebula, *Astron. Lett.,* 2023, vol. 49, p. 65.
41. Lyubarsky, Y.E., On the structure of the inner Crab nebula, *Mon. Not. R. Astron. Soc.,* 2002, vol. 329, p. L34.
42. Michel, F.C., Rotating magnetospheres: an exact 3-D solution, *Astrophys. J.,* 1973, vol. 180, p. L133.
43. Ponomaryov, G.A., Levenfish, K.P., and Petrov, A.E., Jet and counter-jet in transonic pulsar wind nebulae, *J. Phys.: Conf. Ser.,* 2021, vol. 2103, p. 012021.
44. Hester, J.J., Mori, K., Burrows, D., Gallagher, J.S., Graham, J.R., Halverson, M., Kader, A., Michel, F.C., and Scowen, P., Hubble space telescope and Chandra monitoring of the Crab synchrotron nebula, *Astrophys. J.,* 2002, vol. 577, p. L49.
45. Komissarov, S.S. and Lyutikov, M., On the origin of variable gamma-ray emission from the Crab nebula, *Mon. Not. R. Astron. Soc.,* 2011, vol. 414, p. 2017.
46. Chevalier, R.A. and Reynolds, S.P., Pulsar wind nebulae with thick toroidal structure, *Astrophys. J.,* 2011, vol. 740, p. L26.
47. Levenfish, K.P., Ponomaryov, G.A., Petrov, A.E., Bykov, A.M., and Krassilchtchikov, A.M., Slow motion pulsar wind nebulae, *J. Phys.: Conf. Ser.,* 2021, vol. 2103, p. 012020.

48. Fateeva, S.S., Levenfish, K.P., Ponomaryov, G.A., Petrov, A.E., and Fursov, A.N., On the nature of the bar-shaped X-ray feature in the Lee jet of the Vela pulsar wind nebula, *Astron. Lett.,* 2023, vol. 49, p. 56.
49. Petrov, A.E., Levenfish, K.P., and Ponomaryov, G.A., Reverberation of the Vela pulsar wind nebula, *Astron. Lett.,* 2023, vol. 49, p. 777.
50. Bykov, A.M., Amato, E., Petrov, A.E., Krassilchtchikov, A.M., and Levenfish, K.P., Pulsar wind nebulae with bow shocks: non-thermal radiation and cosmic ray leptons, *Space Sci. Rev.,* 2017, vol. 207, p. 235.
51. Meyer, D.M.A., Meliani, Z., Velazquez, P.F., Pohl, M., and Torres, D.F., On the plerionic rectangular supernova remnants of static progenitors, *Mon. Not. R. Astron. Soc.,* 2024, vol. 527, p. 5514.
52. Mignone, A., Bodo, G., Massaglia, S., Matsakos, T., Tesileanu, O., Zanni, C., and Ferrari, A., PLUTO: A numerical code for computational astrophysics, *Astrophys. J.: Suppl. Ser.,* 2007, vol. 170, p. 228.
53. Lyubarsky, Y.E., The termination shock in a striped pulsar wind, *Mon. Not. R. Astron. Soc.,* 2003, vol. 345, p. 153.
54. Komissarov, S.S., Magnetic dissipation in the Crab nebula, *Mon. Not. R. Astron. Soc.,* 2013, vol. 428, p. 2459.
55. Cerutti, B., Philippov, A.A., and Dubus, G., Dissipation of the striped pulsar wind and nonthermal particle acceleration: 3D PIC simulations, *Astron. Astrophys.,* 2020, vol. 642, p. A204.
56. Bogovalov, S.V., Khangulyan, D.V., Koldoba, A.V., Ustyugova, G.V., and Aharonian, F.A., Modelling interaction of relativistic and non-relativistic winds in binary system PSR B1259-63/SS2883 – I. Hydrodynamical limit, *Mon. Not. R. Astron. Soc.,* 2008, vol. 387, p. 63.